Recombination Reactions of Oxygen Atoms on an Anodized Aluminum Plasma Reactor Wall, Studied by a Spinning Wall Method

P. F. Kurunczi,[†] J. Guha, and V. M. Donnelly*

Department of Chemical Engineering, University of Houston, Houston, Texas 77204

Received: July 28, 2005; In Final Form: September 9, 2005

We have studied the recombination of O atoms on an anodized Al surface in an oxygen plasma, using a new "spinning wall" technique. With this method, a cylindrical section of the wall of the plasma reactor is rotated and the surface is periodically exposed to an oxygen plasma and then to a differentially pumped mass spectrometer (MS). By varying the substrate rotation frequency (r), we vary the reaction time (t_r), that is, the time between exposure of the surface to O atoms in the plasma and MS detection of desorbing O_2 ($t_r = 1/2r$). As t_r is increased from 0.7 to 40 ms, the O_2 desorption signal decreases by a factor of 2 for an O-atom flux of 1×10^{16} cm^{-2} s^{-1} and by a factor of 6 when the O flux is 1×10^{17} cm^{-2} s^{-1}. The O_2 signal decay is highly nonexponential, slowing at longer times and reaching zero signal as $r \rightarrow 0$. A model of O-atom recombination is compared with these time-dependent results. The model assumes adsorption occurs at surface sites with a range of binding energies. O can detach from these sites, become mobile, and diffuse along the surface. This leads to desorption of O, reattachment at free adsorption sites, and recombination to form O_2 that promptly desorbs. With several adjustable parameters, the model reproduces the observed shapes of the O_2 desorption decay curves and the lack of detectable desorption of O and predicts a high O-atom recombination coefficient on anodized aluminum.

1. Introduction

The widths of features on silicon integrated circuits are currently as small as ∼80 nm and will become even smaller in the coming decades, allowing ever more and faster transistors to be packed into these devices. Plasma processing is one of the cornerstone technologies that has made and continues to make this evolution possible.[1,2] Chemistry-rich plasmas are widely used to deposit thin films such as silicon dioxide, silicon nitride, and amorphous silicon, but the greatest contribution of plasma processing to the field is in transferring patterns from photolithographically defined films into underlying layers. This plasma process can etch fine-line features into silicon, SiO_2, aluminum, and other microelectronics materials with complete fidelity, due to the highly anisotropic ion bombardment of the surface at normal incidence.

Despite its success, plasma etching is not an easily controlled process. This is due to the complex mix of neutral radicals and positive ions in the plasma and their coupled reactions on the surface of the material that is being etched. Although many years of research in this and related fields such as combustion chemistry and atmospheric chemistry has led to a fairly detailed understanding of the gas-phase plasma chemistry, considerably less is known about the important surface reactions. Radicals including O, Cl, F, and CF_2 are formed by fragmentation of feed gases such as O_2, Cl_2, and CF_4 resulting from collisions with electrons in the plasma. In the presence of energetic ion bombardment, these species react with Al, Si, SiO_2, polymers, and other integrated circuit materials to form volatile products. Control of the concentration of these and other reactants is critical for controlling the etching rate, etched feature sidewall angle, and line width, both over time (reproducibility) and as a

function of position across large (e.g., 12 in. diameter) Si wafers (uniformity).[3−5] This becomes more and more difficult as the feature sizes continue to shrink.

Radical densities in these plasmas are controlled by the balance between formation and loss reactions. Radicals are lost by reactions that form etching products, by wall reactions such as recombination, or by being pumped away. In addition to formation by electron impact, larger radicals are also formed by association reactions of smaller radicals on the wall of the plasma chamber.[5−8] Because the pressure in most plasma etching processes is quite low (typically ∼5−100 mTorr), three-body gas-phase association reactions are very slow. Most gas-phase atom exchange reactions are also too slow at these low number densities. Therefore, the majority of the important neutral−neutral reactions in plasma etching occur on the walls of the chamber, or on the wafer. These heterogeneous reactions are generally not well understood or controlled. This is exacerbated by the fact that the wall conditions can change over time (even over the roughly 1 min etching process) and are a strong function of the recent history of the chamber.

One important class of surface reactions is atom recombination such as $2O(g) \xrightarrow{\text{wall}} O_2(g)$, which is a major loss process for O atoms in oxygen-containing plasmas. The highly variable nature of the surface is mainly responsible for the fact that atom recombination rates and hence number densities can vary widely in plasmas with otherwise identical conditions (feed gases, pressures, power densities, etc.). Due to the complex nature of the surface, it is very difficult to compute the probability for even such "simple" reactions as atom recombination. Likewise, it is a sizable challenge to measure the rate directly, in situ. Consequently, surface recombination coefficients (the probability per collision with the surface that an impinging radical will recombine) and sticking coefficients are often obtained from

† Present affiliation: Varian Semiconductor Equipment, Gloucester, MA 01930.

experiments in which surfaces in high vacuum are exposed to a beam of atoms or small radicals to partially simulate plasmas conditions.[9-12] While these studies provide valuable information on recombination under simpler conditions, in the complex plasma environment, the reactor walls are bombarded by moderate energy (~10 eV) ions and low energy electrons with fluxes of typically 10^{16} cm^{-2} s^{-1}, in addition to high fluxes of products such as SiCl and CF, which can readily deposit on the surface. These added complications can drastically alter the heterogeneous chemistry.

To characterize the surface layer on reactor walls, other researchers have looked at surfaces in situ by total internal reflection Fourier transform IR (TIR-FTIR) spectroscopy,[13,14] and laser-induced thermal desorption,[15-18] or after plasma exposure by vacuum-sample-transfer X-ray photoelectron spectroscopy (XPS).[19-24] While yielding information on the buildup and removal of surface species, these methods do not provide recombination coefficients, sticking coefficients, or surface kinetics. The TIR-FTIR method is also limited to IR-transparent surfaces such as GaAs, as opposed to the more common reactor materials, anodized aluminum and SiO_2. It is therefore difficult to prepare a representative surface for study outside of the plasma, or to carry out kinetic measurements on a surface directly in the plasma. Consequently, new approaches are needed to study surfaces under dynamic plasma conditions during exposure to multiple reactants. These methods should provide the quantitative kinetic data (sticking coefficients, recombination probabilities, reaction probabilities and branching ratios, activation energies, pre-exponential factors, reaction orders, etc.) that are largely lacking in computer models. Accurate predictions from these models will increasingly be relied upon to aid the optimization of plasma processes and equipment that will be needed to meet future etching demands.[25]

Previously, we reported a new approach to the study of complex plasma wall reactions.[26] A cylindrical substrate coated with the material of interest (e.g., anodized aluminum, a common chamber coating in plasma reactors) is embedded in the wall of the reactor and is spun at a rapid rate (up to 200 000 rpm). The surface is periodically exposed to the plasma and then to a mass spectrometer in an opposing differentially pumped chamber. Conical skimmers close to the spinning substrate allow the pressure in the plasma chamber to be relatively high, while maintaining low pressures in the differentially pumped chambers. By varying the rotation frequency, we can vary the time between exposure to the plasma and detection of products desorbing from the surface, thus making it possible to derive reaction kinetics. In the present study, we have investigated the desorption of O_2 from aluminum oxide (i.e., oxygen plasma exposed anodized Al) following heterogeneous recombination of O atoms in an oxygen plasma and developed a multisite adsorption model to explain the observations.

2. Experimental Procedure

The apparatus for these studies is depicted in Figures 1 and 2. The plasma reactor consists of a water-cooled inductively coupled plasma source. The chamber is anodized aluminum, with quartz viewports. Anodized aluminum inserts cover short, stainless steel flanges that are bonded to the aluminum chamber. The spinning substrate (anodized aluminum in this case) is shown in Figure 1 and in more detail in Figure 2. The substrate is rapidly rotated by a brushless motor (Koford) with ceramic bearings. The motor is designed to operate at a top speed of 201 600 rpm but was not taken above 40 000 rpm in these
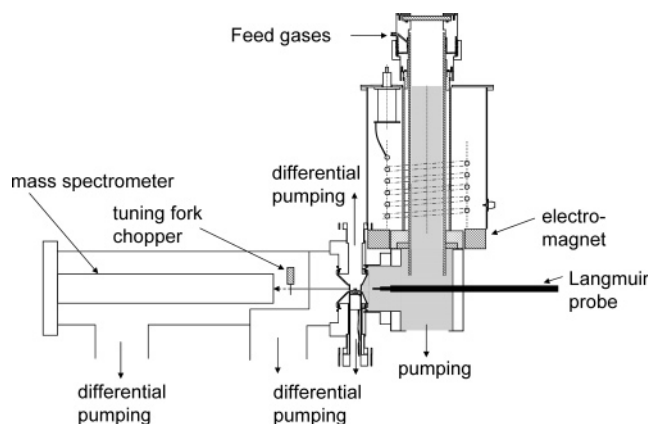

Figure 1. Experimental system, including an inductively coupled plasma reactor and a differentially pumped line-of-sight mass spectrometer. The plasma and intermediate chambers are separated by the wall that contains the rotating anodized Al substrate. Not shown is the configuration for line-of-sight mass spectrometric sampling of the plasma neutrals and positive ions, made possible by replacing the cylinder and skimmers with two aperture plates.

studies. Despite its light weight, the substrate required balancing for operation at higher speeds.

The spinning substrate is housed in a stainless steel chamber (HIS Corp), depicted in more detail in the cross-sectional side view in Figure 2. Conical skimmers on both sides closely follow the contour of the cylindrical rotating substrate with a constant spacing of about 100 μm. The skimmer on the side facing the plasma reactor is made of anodized aluminum. The substrate chamber is differentially pumped from both sides and from the bottom, allowing a pressure of 1×10^{-5} Torr to be achieved inside this chamber when the pressure in the plasma chamber is 10 mTorr. The substrate chamber is connected to an intermediate chamber that is differentially pumped with a 500 L/s turbomolecular pump. The pressure in this chamber is 3×10^{-8} Torr when the plasma chamber pressure is 10 mTorr. A third differentially pumped (1000 L/s cryopump) chamber houses a quadruple mass spectrometer (Extrel, 0−400 amu) and a 103 Hz tuning fork chopper. When the plasma chamber pressure is 10 mTorr, the pressure rise in the mass spectrometer chamber is ~1×10^{-10} Torr.

The mass spectrometer ionizer was operated at an electron energy of 70 eV and a current of 5 mA. A 2 mm diameter aperture at the front of the ionizer is line-of-sight with the center of the chopper window, the 4.7 mm diameter aperture separating the second and third differentially pumped chambers, and the center of the 10 mm diameter aperture in the stainless steel cone on the analysis side of the spinning substrate chamber. When the chopper is in the open position, the mass spectrometer signal consists of a beam component of species desorbing from the line-of-sight substrate, a collimated background component (discussed below), and an isotropically scattered background gas in the mass spectrometer chamber. In the chopper-closed position, only the isotropically scattered background gas is detected. Mass spectrometer signals are recorded in a pulse counting mode, with a gated pulse counter (SRI model 400). Equal length (2 ms) gates overlap the fully open and fully closed chopper positions. These signals are used for the extraction of net line-of-sight components of signals (chopper-open minus chopper-closed signals).

The procedure for data collection is as follows. First, with the plasma off and gas flowing, mass spectrometer measurements are recorded as a function of substrate rotation frequency (r). Measurements are then made as a function of substrate
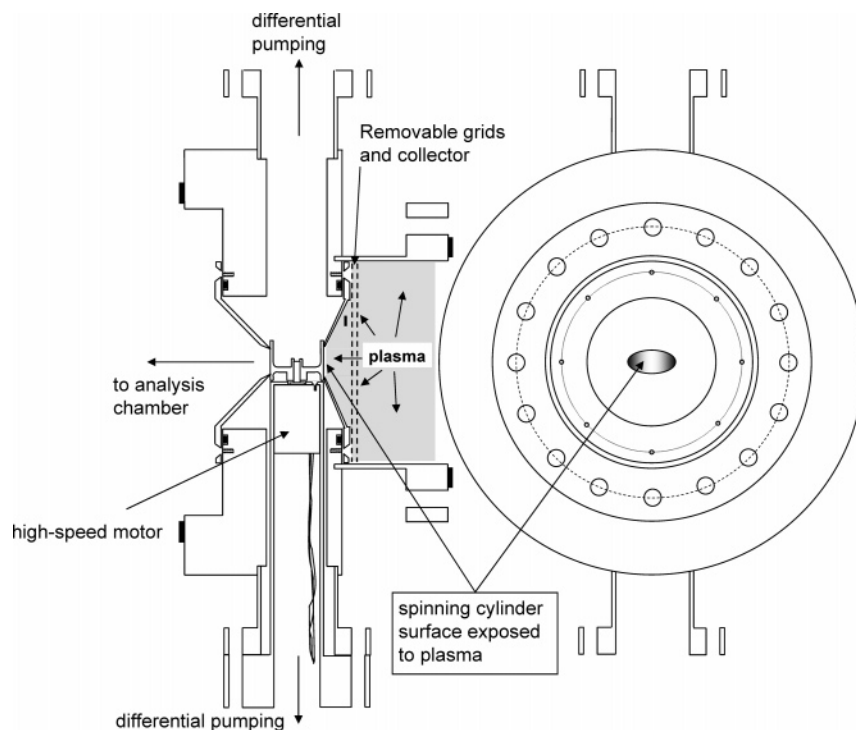
Figure 2. Detailed side view (left) and view from the plasma (right) of the hollow chamber wall containing the rotating cylindrical substrate and conical skimmers.

rotation frequency with the plasma on. Any net increase in signal above the background is due to species that are desorbing from the substrate surface when it has rotated from the plasma to the position facing the mass spectrometer. At the highest rotation frequencies investigated in this study, this time was 0.75 ms. The temperature of the substrate is measured through a ZnSe window with a pyrometer. Experiments were carried out at temperatures between room temperature and 36 °C. This upper temperature is reached after a period of time that depends on motor rotation speed and plasma power. The sample is allowed to cool between sets of measurements.

Dual grids in the plasma adjacent to the spinning substrate can be biased to prevent positive ion bombardment (Figure 2). A small collector behind the grids and next to the substrate is used to verify rejection of the positive ions. These grids can also be used with the collector to record ion energy distributions. Since the grids were each 70% open area and were aligned, they allowed between 50% and 70% of the uncharged species (e.g., O atoms) to pass through. Most experiments were carried out with the grids removed.

Several methods were also used to characterize the oxygen plasma. A movable Langmuir probe[27] was used to measure ion and electron densities, electron temperatures (T_e), and potentials across the plasma to within ~5−10 mm of the wall. In some experiments, the spinning substrate was replaced with two aperture plates to allow line-of-sight mass spectrometric sampling of O-atom fluxes at the wall. Optical emission spectroscopy was also used to characterize the plasma but will not be discussed here. The anodized aluminum surface is cleaned and conditioned by hours-long exposure to the oxygen plasma during the course of the experiments.

3. Results and Discussion

3.1. General Considerations on the Interpretation of Signals. With O_2 flowing through the chamber and the plasma off, signals are detected by the mass spectrometer at $m/e = 32$

with the chopper in the open and closed positions with the cylinder at rest. The O_2 signal with the chopper closed is due to the gas that leaks around the skimmers and scatters in the chambers (L_s^{off}). The chopper-open signal is larger than the chopper-closed signal, indicating that the mass spectrometer also receives a line-of-sight beam flux of gas that leaks around the second skimmer. A ray trace of the geometry of the system indicates that this contribution lies within the penumbra formed by the fourth aperture on the mass spectrometer ionizer and the third aperture that separates the mass spectrometer chamber from the intermediate chamber. The leak beam component with the plasma off (L_b^{off}) is given by the difference in the plasma-off−chopper-open (PFCO) and plasma-off−chopper-closed (PFCC) signals:

$$L_b^{off} = \text{PFCO} - \text{PFCC} \qquad (1)$$

With the plasma off, small increases (20−30%) in chopper-open and chopper-closed O_2 signals are observed as the rotation frequency increases from 0 to 35 000 rpm. This is due to O_2 that is dragged into the wall chamber and is likely enhanced by the rough nature of the anodized Al surface. When the substrate is not rotating, the O_2 signals with the chopper open and closed are unchanged when a plasma is ignited. When the substrate is rotated with the plasma on, however, both signals increase strongly with rotation speed. The plasma-on−chopper-open (POCO) signal contains contributions from the line-of-sight beam desorbing gas (D_b^{on}), the line-of-sight beam leak (L_b^{on}), the scattered leak (L_s^{on}), and the scattered desorbing species (D_s^{on}). The plasma-on−chopper-closed (POCC) signal is composed of L_s^{on} and D_s^{on}. Consequently, the difference in signals gives the beam component signals:

$$D_b^{on} + L_b^{on} = \text{POCO} - \text{POCC} \qquad (2)$$

The leak beam component with the plasma on is related to the

leak components with the plasma off by

$$L_b^{on} = (f^{on}/f^{off})L_b^{off} \qquad (3)$$

where f^{off} is the O_2 flux through the space between the substrate and the skimmer on the plasma chamber with the plasma off and f^{on} is the flux of O_2 plus twice the flux of O through this space with the plasma on. This is assuming that all O entering the wall chamber recombines during one of several collisions with the mostly stainless steel surfaces to form O_2 before leaking through the space between the substrate and second skimmer. We determine f^{on}/f^{off} with no rotation of the substrate ($r = 0$) from

$$f^{on}/f^{off} = (POCO - POCC)_{r=0}/(PFCO - PFCC)_{r=0} \quad (4)$$

f^{on}/f^{off} values were determined at $m/e = 32$. Finally, the desired signal, due just to the product O_2 desorbing from the spinning substrate, is given by

$$D_b^{on} = POCO - POCC - (f^{on}/f^{off})(PFCO - PFCC) \quad (5)$$

Values for f^{on}/f^{off} were very close to 1 (0.967 ± 0.015) at the highest power (600 W). This indicates that the temperature of the plasma neutrals (mostly O_2) near the wall is not much higher than the wall temperature. Since f^{on}/f^{off} will be even closer to 1 at lower powers, we assumed $f^{on}/f^{off} = 1$ in all cases.

3.2. Identification of Reactants and Products. The net signal (D_b^{on}) at $m/e = 32$ is a result of electron impact ionization of O_2 in the mass spectrometer ionizer. O_3 as a desorption product, cracking to form O_2^+ in the mass spectrometer, can be conclusively ruled out, since its parent ion is not observed at $m/e = 48$.[26] All of the signal at $m/e = 16$ can be attributed to the cracking of O_2 in the mass spectrometer, indicating that no significant desorption of O occurs ($< \sim 5\%$ of the amount of O_2 that desorbs). No signals are observed with the mass spectrometer ionizer off.[26] The only plausible explanation for the desorption of O_2 is the recombination of O atoms. O^- in the plasma cannot reach the substrate, due to the repelling sheath potential. We have also ruled out the possibility that O_2^+ bombarding the surface could become briefly entrained in the near-surface region, leading to O_2 desorption over ~ 40 ms.[26]

Here, we present a more detailed description of the experiments that show that ion bombardment does not affect the O_2 desorption signal. Dual stainless steel grids were placed in front of the substrate to repel positive ions (see Figure 2), while allowing O atoms to reach the substrate at a reduced flux. Each grid had a 70% open area; hence, the two grids will reduce the flux of O atoms by 50% assuming a high recombination rate on stainless steel. (Although the grids' holes were aligned and therefore transmitted close to 70% at normal incidence to the grid planes, the wide angular spread of the O-atom flux makes this largely irrelevant.) The first grid was used to repel electrons, and the highly positively biased second grid stops ions from reaching the substrate. A small grounded collector electrode was placed near the substrate behind the second grid to measure ion current and ensure that positive ions were prevented from reaching the substrate. We could also use this setup to obtain ion energy distributions (IEDs).

A typical current−voltage ($I−V$) and IED measurement is presented in Figure 3. Because of the high percentage of insulating surfaces in this plasma reactor, the floating potential (V_f) is quite high (e.g., $+40$ V for 2.5 mTorr and 200 W). We therefore found that a *positive* potential of $V_1 = 20$ V on the first grid was sufficient to repel most of the electrons. The
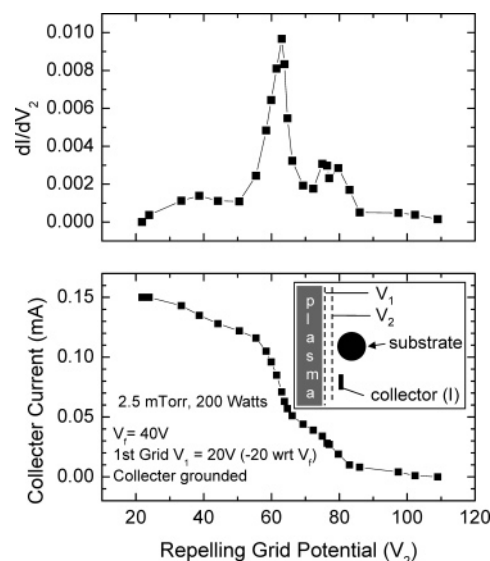

Figure 3. Ion current measurements as a function of repeller voltage V_2 on the second grid (see inset) at the spinning substrate for an O_2 plasma at 2.5 mATorr and 200 W. The potential V_1 on the first grid of 20 V (-20 V with respect to the plasma floating potential) repelled most of the electrons. dI/dV_2 provides an ion energy distribution (with respect to ground potential) at the spinning wall.

second grid potential was swept from 20 to 110 V. Current (i.e., ion current) as a function of the repeller grid voltage is shown in the bottom portion of Figure 3. The ion current drops to near-zero at $V_2 = 100$ V. The relative IED (dI/dV_2), also shown in Figure 3, reveals two peaks at 63 and 78 eV (with respect to ground). The substrate spends 35% of the time in the plasma; therefore, it receives 35% of the ion and electron flux (with the grids removed) of an electrically floating object at the chamber wall. Since the floating potential is not a strong function of plasma density, we might expect the potential of the surface of the spinning substrate on the midpoint circumference would be close to $+40$ V. Several complicating effects, including conductivity of the aluminum oxide layer and leakage paths through the cylinder, motor shaft, and bearings to ground, could reduce the substrate floating potential. Assuming the substrate floating potential is 40 V, the energy of ions striking the substrate with the grids removed or floating under these conditions is ~ 30 eV.

Figure 4 presents measurements of chopper-open minus chopper-closed signals at $m/e = 32$ with $V_2 = 0$ V on grid #2 to allow positive ions to reach the substrate (collector ion current 145 μA), or with $V_2 = 100$ V to block positive ions from reaching the substrate (collector ion current 2 μA). The difference between these two conditions is barely distinguishable, indicating that positive ions do not contribute significantly to the signals at $m/e = 32$. These fixed rotation speed measurements were carried out at other pressures with similar results. Measurements were carried out at higher power (600 W) and as a function of rotation frequency for a 5 mTorr O_2 plasma (Figure 5). V_1 was -150 V, and V_2 was set at $+55$ V, reducing the ion collector current from 140 μA (with the grids grounded) to ~ 20 uA. (It was not possible to apply higher V_2 bias and further reduce the ion current without igniting a plasma behind the grids at this high power.) Within the scatter of the measurements, the two sets of data are nearly indistinguishable. Furthermore, the same result is obtained if the grids are allowed to electrically float. These measurements indicate that positive ion bombardment has no appreciable effect on the O_2 signals.

Recombination Reactions of Oxygen Atoms

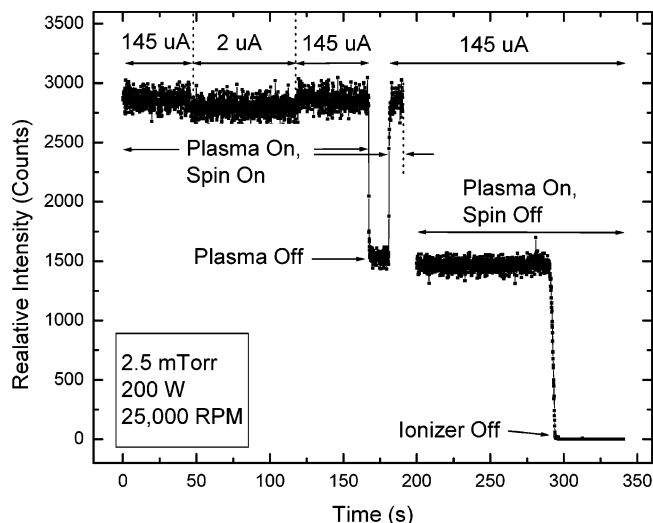*J. Phys. Chem. B, Vol. 109, No. 44, 2005* **20993**

Figure 4. Chopper-open minus chopper-closed signal at $m/e = 32$ as a function of time with the plasma on and off and grid #2 either biased ($V_2 = 100$ V) to allow only neutrals (O, O_2) to impinge on the substrate or grounded to allow neutrals and positive ions (mostly O_2^+) to impinge. Rotation frequency 25 000 rpm.
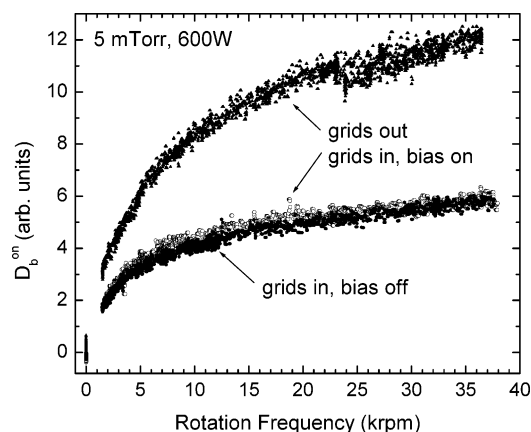

Figure 5. D_b^{on} for O_2 vs rotation frequency for a 5 mTorr, 600 W O_2 plasma, with and without grids between the plasma and the rotating substrate. Solid triangles, no grids; solid circles, unbiased grids; open circles, biased grids (first grid at −150 V, second grid at +55 V) to repel positive ions and electrons. No bias, 140 μA collector current; with above bias conditions, ~20 μA collector current and collector grounded.

Figure 5 also shows measurements with the grids removed. The shape of the curve is similar to that with the grids in place, but the signal is about twice as large. As discussed above, a 50% reduction in O-atom flux is expected with the two grids in place; thus, a factor of 2 larger signal with the grids removed is reasonable. Finally, in experiments with Ar plasmas at 600 W, an Ar desorption signal is not observed, ruling out a process in which Ar$^+$ is briefly implanted, leading to delayed desorption of Ar. This lends further support to the conclusion that O_2^+ and/or O$^+$ is not the reactant responsible for the formation and desorption of O_2.

3.3. Time, Power, and Pressure Dependencies. Figure 6 shows a typical set of measurements of the net signal of desorbing O_2 (D_b^{on}) computed from eq 5 versus substrate rotation frequency (in thousands of rotations per minute, krpm) as a function of power at 1.25 mTorr. These types of measurements can be plotted as a function of the reaction observation time, defined as the time it takes for a point on the surface to rotate from the midpoint of plasma exposure at $\theta = 0$ (see Figure
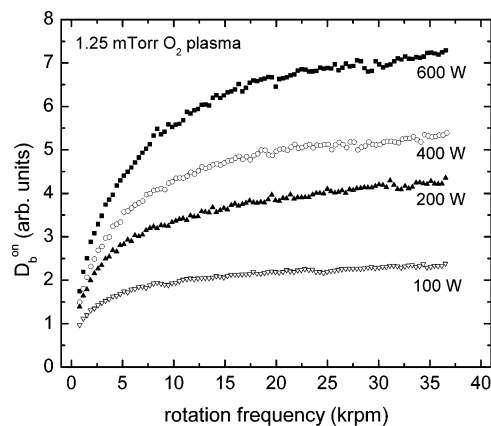

Figure 6. D_b^{on} for O_2 vs the substrate rotation frequency for a 1.25 mTorr O_2 plasma, as a function of power. No grids were present between the sample and the plasma.
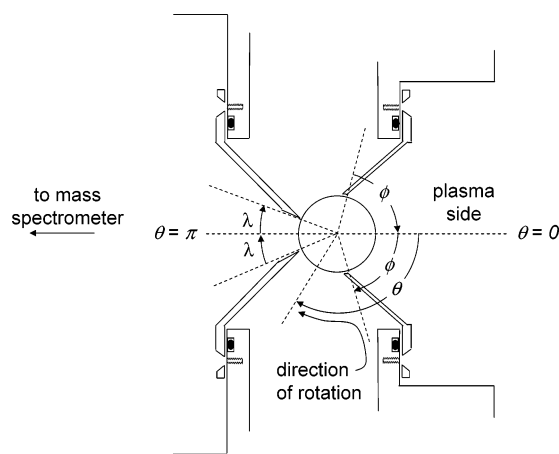

Figure 7. Rotating substrate geometry and angles used to define reaction time for the measurements and in the simulations. $\phi = 63°$, $\lambda = 22°$.
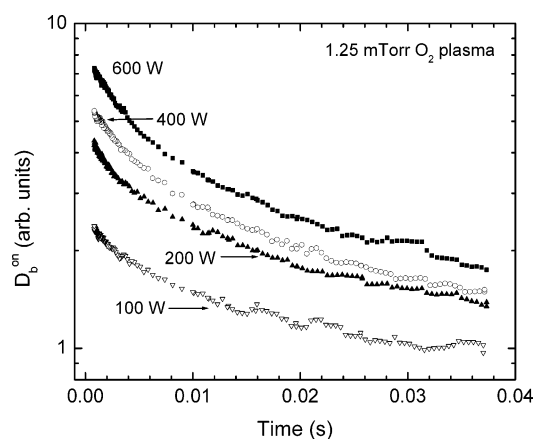

Figure 8. D_b^{on} for O_2 vs reaction time (reciprocal of twice the rotation frequency) for a 1.25 mTorr O_2 plasma, as a function of power, derived from the data in Figure 8. No grids were present between the sample and the plasma.

7) to the midpoint of the region seen by the mass spectrometer ($\theta = \pi$), that is, the reciprocal of twice the rotation frequency. Plots of the logarithmic dependence of D_b^{on} on reaction time are presented as a function of pressures and power for 1.25, 2.5, 5, 10, and 20 mTorr in Figures 8−12, respectively. The rate of decay of O_2 desorption is rapid at short times and slower at longer times. At each pressure, the decay rate is also faster at higher power and shorter times.
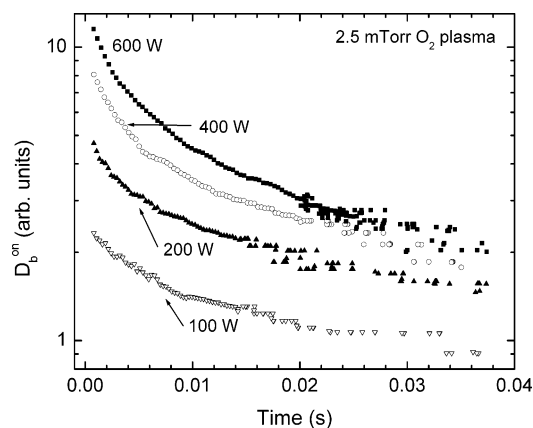
Figure 9. D_b^{on} for O_2 vs reaction time (reciprocal of twice the rotation frequency) for a 2.5 mTorr O_2 plasma, as a function of power. No grids were present between the sample and the plasma.

Figure 10. D_b^{on} for O_2 vs reaction time (reciprocal of twice the rotation frequency) for a 5 mTorr O_2 plasma, as a function of power. No grids were present between the sample and the plasma.
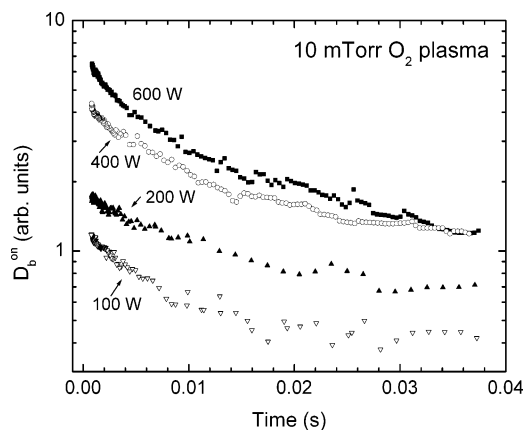
Figure 11. D_b^{on} for O_2 vs reaction time (reciprocal of twice the rotation frequency) for a 10 mTorr O_2 plasma, as a function of power. No grids were present between the sample and the plasma.
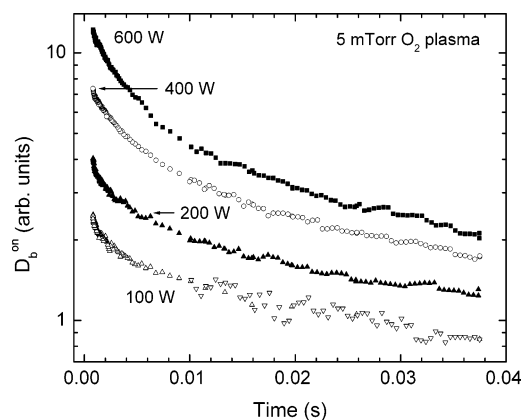
3.4. Plasma Characterization Measurements.
3.4.1. Absolute O-Atom Densities Adjacent to the Substrate. We also carried out measurements to characterize the plasma adjacent to the spinning substrate. O-atom densities were measured by removing the substrate and replacing the conical skimmers with two flat aperture plates. The mass spectrometer monitored $m/e = 16$ and 32 with the chopper open and closed. When O_2 is present in the reactor and the plasma is off, the signal is almost entirely due to the line-of-sight flux from the plasma (chopper-open/chopper-closed = 20:1). Sample differ-

Figure 12. D_b^{on} for O_2 vs reaction time (reciprocal of twice the rotation frequency) for a 20 mTorr O_2 plasma, as a function of power. No grids were present between the sample and the plasma.
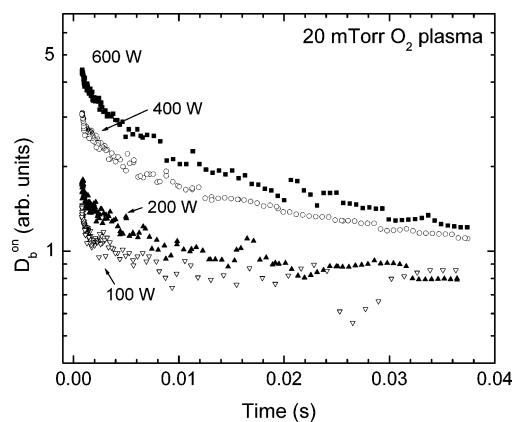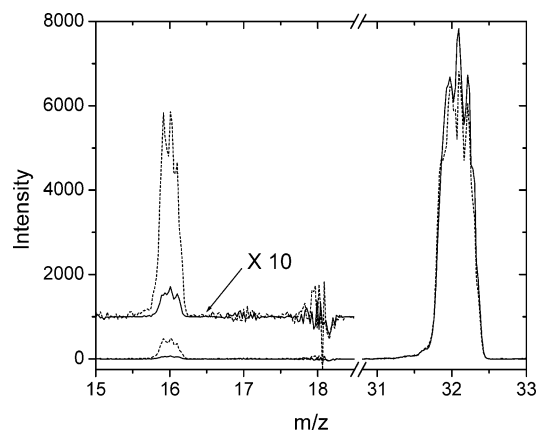

Figure 13. Chopper-open minus chopper-closed mass spectra of the line-of-sight number densities in the plasma at the wall, with the spinning substrate removed and the two conical skimmers replaced with aperture plates. Pressure 1.25 mTorr. Mass spectrometer ionization energy 25 eV. Solid line, plasma off; dashed line, plasma power of 600 W.

ence spectra (chopper-open minus chopper-closed) are shown in Figure 13 for the plasma on and off. The $m/e = 32$ peak decreases by a small amount and the $m/e = 16$ peak increases when the plasma is turned on, due to the dissociation of O_2 and the formation of O. A small amount (1.0%) of Ar was also added to account for reductions in number densities due to heating of the gas. The Ar number density decreased by 20% at 2.5 mTorr when the plasma was ignited at the highest power (600 W), indicating a gas temperature of about 350 K if all of this effect is due to heating of the gas. At 20 mTorr, no decrease in Ar, and hence rise in temperature, is observed at any power. Consequently, we assumed that the gas near the wall was at the wall temperature in all cases.

Following the procedure described elsewhere for line-of-sight mass spectrometric sampling of a chlorine plasma,[28] the O-to-Ar number density measurements presented in Figure 14 were recorded for the conditions used in this study. Cross sections of 0.53 (the average of four reported values[29-32]), 0.46 (average of three values[32-34]), and 1.25 (Freund and co-workers[35]) were used for electron impact ionization of O, O_2, and Ar, respectively, at 25 eV. The corresponding O-atom fluxes (f_O) are given in Table 1.

3.4.2. Langmuir Probe Measurements. Electron densities (n_e) measured with the Langmuir probe are summarized in Table 1. In these measurements, the probe was scanned across the plasma, extending as close as possible to the aperture plate
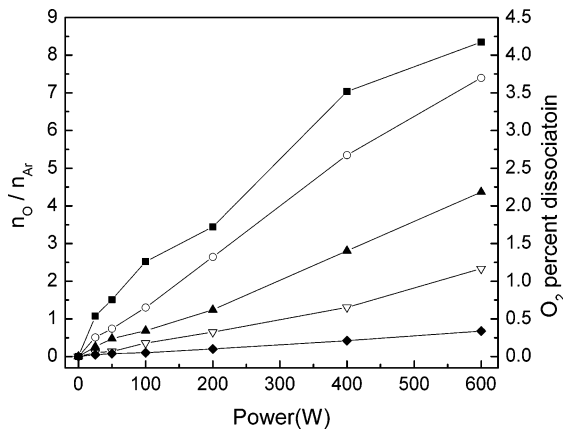
Recombination Reactions of Oxygen Atoms

J. Phys. Chem. B, Vol. 109, No. 44, 2005 **20995**

Figure 14. O-to-Ar number density ratios at the plasma reactor wall, for 1% Ar/O_2 plasmas, measured by line-of-sight mass spectrometry.

TABLE 1: Plasma Characterization Measurements (O-Atom Flux = f_O (10^{16} cm^2 s^{-1}). Electron Density = n_e (10^{10} cm^3) near (~5−10 mm from) the Wall, and the Maximum Density near the Center of the Plasma)

power (W)		1.25	2.5	5	10	20
		pressure (mTorr)				
100	f_O	1.49	1.54	1.62	1.68	0.98
	n_e (wall)		0.11	0.085	0.078	0.057
	n_e (max)		0.46	0.45	0.43	0.32
200	f_O	2.04	3.12	2.93	3.08	1.89
	n_e (wall)	0.24	0.22	0.13	0.15	0.10
	n_e (max)	0.75	0.86	0.76	0.69	0.49
400	f_O	4.16	6.32	6.63	6.17	4.02
	n_e (wall)	0.40	0.46	0.42	0.35	0.20
	n_e (max)	1.29	1.69	1.58	1.42	0.85
600	f_O	4.93	8.74	10.3	11.0	6.41
	n_e (wall)	0.74	0.93	0.85	0.72	0.23
	n_e (max)	1.93	2.71	2.71	2.71	1.75

TABLE 2: Multisite Adsorption Model for O-Atom Surface Recombination ($\bar{v}_O$ Is the O(g) Thermal Speed near the Wall (Assumed to be the Wall Temperature))

	rate constant
(1) O(g) + S(i) → O(i)	$s(i)\bar{v}_O/4$
(2) O(g) → O_m	$s_m\bar{v}_O/4$
(3) O(i) → O(g) + S(i)	$k_{da}(i) = A_{da} \exp[-E_{ba}(i)/RT]$
(4) O_m → O(g)	$k_{dm} = A_{dm} \exp[-E_{bm}/RT]$
(5) O(i) → O_m + S(i)	$k_m(i) = A_m \exp[-E_m(i)/RT]$
(6) $2O_m$ → O_2(g)	$k_{mm} = D_0 \exp[-E_{mm}/RT]P_{mm}$
(7) O_m + O(i) → O_2(g) + S(i)	$k_{ma}(i) = D_0 \exp[-E_{mm}/RT]P_{ma}$ $\exp[-E_{ma}(i)/RT]$
(8) O_m + S(i) → O(i)	$k_{mS} = D_0 \exp[-E_{mm}/RT]P_{mS}$ $\exp[-E_{mS}/RT]$

(within ~5−10 mm). Electron energy distributions were generally non-Maxwellian, especially at higher pressures and lower powers near the wall, and will not be presented here.

3.5. General Discussion of the Time Dependence of Desorption Signals. To extract kinetic data from the results in Figures 8−12, we have evaluated two models. A simple Langmuir−Hinshelwood model described previously did not reproduce the measurements very well.[26] Here, we invoke the more detailed mechanism for recombination of oxygen atoms on anodized aluminum presented in Table 2. The mechanism is similar to that described by Kim and Boudart[36] and Cartry et al.[37] for recombination of O atoms on silica. O(g) adsorbs (reaction 1) at binding sites ($S(i)$) with a distribution of binding energies ($E_{ba}(i)$) to form relatively strongly bound O(i). The sticking coefficient for this process ($s(i)$) is assumed to be 1 for open sites. If the site is filled, O(g) can adsorb (reaction 2) as a weakly bound mobile species (O_m) (binding energy E_{bm}).
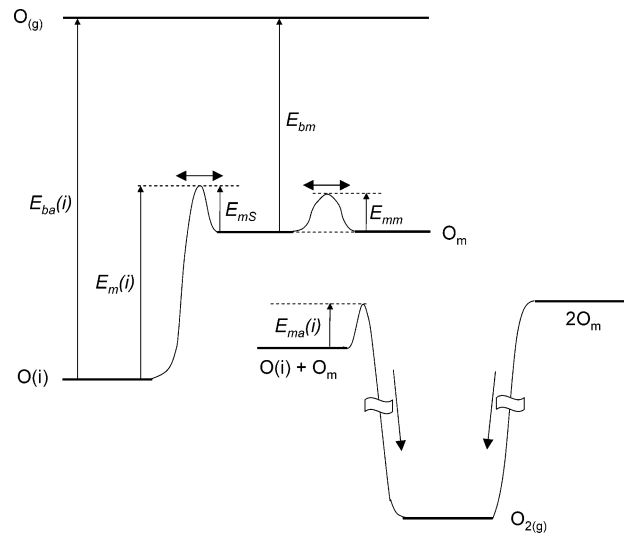

Figure 15. Energy level diagram depicting binding energies and activation energies for the O recombination mechanism in Table 2.

The sticking probability for this process (s_m) was varied (0, 0.5, or 1). O(i) and O_m can desorb (reactions 3 and 4). O(i) can also overcome a activation barrier, $E_m(i)$, to become mobile O_m (reaction 5). O_m diffuses on the surface until it desorbs (reaction 4), recombines with O_m (reaction 6), recombines with O(i) (reaction 7), or binds at a vacant $S(i)$ site (reaction 8). Because $O_m \ll \Sigma$ O(i), reaction 6 is unimportant (see below). Arrhenius expressions are assumed for reactions 3−8. Binding energies and activation barriers are depicted in Figure 15. The parameters listed in Table 2 were allowed to vary subject to the constraint

$$E_{bm} - E_{mS} = E_{ba}(i) - E_m(i) \qquad (6)$$

In addition, we assume that $E_{mS} = E_{mm}$, independent of binding site, and that $E_{ma}(i) = E_{ba}(i)/\alpha$, with the constant $\alpha > 1$.

We assume there are a range of binding energies that we group into n bins. The mean energy of each bin is given by $E_{ba}(i) = E_{ba}(0) + i\Delta_{ba}$, where i is an integer between 1 and n, Δ_{ba} is the constant energy separation, and $E_{ba}(0)$ was assumed to be equal to E_{bm}. The total adsorption site density was assumed to be 1×10^{15} cm^{-3}, distributed with a Gaussian profile over $n = 7$ different binding energies (i.e., coverages × 10^{15} cm^{-2} of 0.0533 for $i = 1$ and 7, 0.124 for $i = 2$ and 6, 0.203 for $i = 3$ and 5, and 0.239 for $i = 4$).

The time dependence of the coverages of O(i) and O_m are given by

$$\frac{d[O(i)]}{dt} = \left(\frac{f_O s(i)}{[S]_0} + k_{mS}(i)[O_m]\right)([S(i)]_0 - [O(i)]) - (k_m(i) + k_{da}(i) + k_{ma}(i)[O_m])[O(i)] \quad (7)$$

$$\frac{d[O_m]}{dt} = \sum_{i=1}^{n}\{k_m(i)[O(i)] - k_{mS}(i)[O_m]([S(i)]_0 - [O(i)]) - k_{ma}(i)[O(i)][O_m]\} + \left(\frac{f_O s_m}{[S]_0}\right)\sum_{i=1}^{n}[O(i)] - (k_{dm} + 2k_{mm}[O_m])[O_m] \quad (8)$$

where $[S(i)]_0$ is the initial density of $S(i)$ sites before exposure to O atoms and $[S]_0$ is the total initial site density (i.e., $[S]_0 = \Sigma[S(i)]_0$). The square brackets indicate coverages, and the rate constants are defined in Table 2. The amounts of O_2 and O
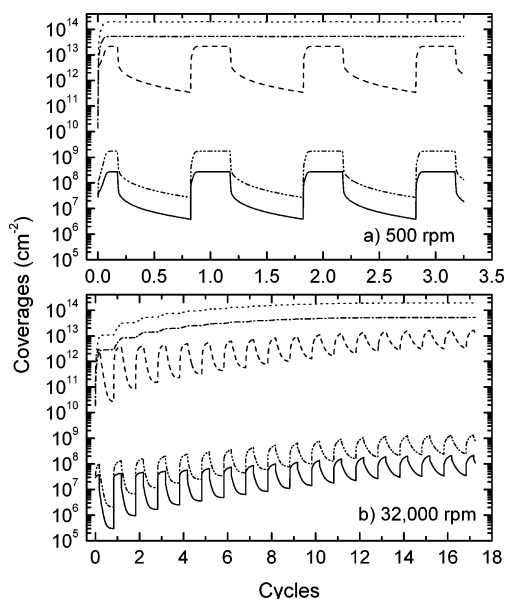
Figure 16. Simulations of the adsorbed O-atom coverage as a function of time. Coverages start at zero and reach their periodic steady states. Parameters in the model are given in Table 3. $f_O = 1 \times 10^{17}$ cm^{-2} s^{-1}. Solid line, O(1); dashed line, O(3); dotted line, O(5); dash−dotted line, O(7); dash−dot−dotted line, O$_m$. (a) Substrate rotation frequency 500 rpm; (b) substrate rotation frequency 32 000 rpm.

desorbing per square centimeter from the surface are given by

$$\frac{d[O_{2(g)}]}{dt} = \sum_{i=1}^{n} k_{ma}(i)[O(i)][O_m] + k_{mm}[O_m]^2 \quad (9)$$

$$\frac{d[O(g)]}{dt} = k_{da}(i)[O(i)] + k_{dm}[O_m] \quad (10)$$

Equations 7−10 were solved by the finite difference method (fourth-order Runge−Kutta with adaptive step size).

Any given point on the substrate midsection (i.e., a point that passes through the centers of the elliptical orifices of the skimmers) is periodically in the plasma for a fraction ϕ/π of each cycle and then removed from the plasma for the remaining fraction of the cycle, as described in Figure 7. Time t is therefore $(1/r)[n + (\theta/2\pi)]$, where n is the number of complete cycles and θ is the phase angle (between 0 and 2π) defined in Figure 7. The O-atom flux at a point on the substrate surface circumference is f for $-\phi < \theta < \phi$ and zero for $\phi < \theta < 2\pi - \phi$.

The desorption measurements recorded in this study were at their steady-state values. To simulate this condition, coverages and desorbing O and O$_2$ must be evaluated until a periodic steady state is reached. The approach to steady state was computed for this mechanism; sample computations of O coverages are presented in Figure 16. At slower rotation rates (e.g., 500 rpm), the depth of modulation of the more weakly bound adsorbates O(1), O(3), and O$_m$ is large and steady state is reached in relatively few cycles. (Steady state in this case is defined as a less than 0.1% change in coverage between $t = n/r$ and $t = (n+1)/r$.) Note the fast and slow components of the decay of coverages each time after the sample leaves the plasma. The coverages of the more strongly bound adsorbates O(5) and O(7) quickly reach their saturation values. These species do not participate in the recombination process. At faster rotation rates (e.g., at 32 000 rpm), O(1), O(3), and O$_m$ are modulated less,
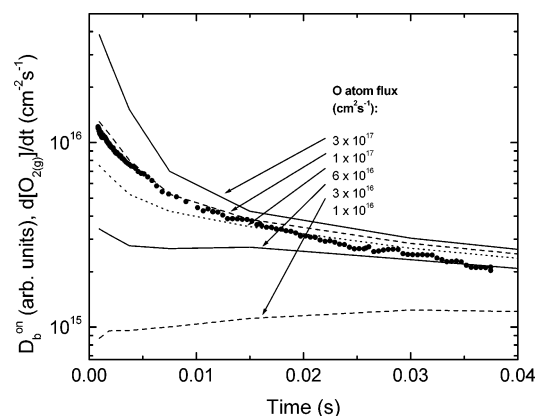

Figure 17. Simulations of steady-state D_b^{on} vs reaction time (reciprocal of twice the rotation frequency) at $\theta = \pi$ for the multisite mechanism in Table 2. Parameters in the model are given in Table 3. A sample set of measurements from Figure 10 (5 mTorr, 600 W) is also included (points). The measurements have been scaled to match the simulation corresponding to an O-atom flux of 1×10^{17} cm^{-2} s^{-1}.

TABLE 3: Binding Energies, Activation Energies, and Pre-exponential Factors for the Multiple Binding Sites ($i = 1-7$) Model in Table 2 and Simulations in Figures 16−18

parameter	value
$s(i)$	1.0
s_m	0.5
$[S]_0$	1×10^{15} cm^{-2}
A_{da}	1×10^{13} s^{-1}
$E_{ba}(i)$	$E_{ba}(i) = E_{ba}(0) + i\Delta_{ba}$ (kcal/mol)
A_m	1×10^{12} s^{-1}
$E_m(i)$	$E_m(i) = E_{ba}(i) + E_{mS} - E_{bm}$ (kcal/mol)
A_{dm}	1×10^{13} s^{-1}
E_{bm}	10 kcal/mol
D_0	5×10^{-4} cm^2 s^{-1}
E_{mm}	2 kcal/mol
P_{mm}	0.5
P_{mS}	1.0
E_{mS}	2 kcal/mol
P_{ma}	0.1
$E_{ma}(i)$	$E_{ba}(i)/10$ (kcal/mol)
Δ_{ba}	3 kcal/mol
$E_{ba}(0)$	E_{bm}

and only the fast decay component is apparent. It also takes more cycles to reach steady state.

Line-of-sight product is detected desorbing from points along the sample midsection at $\pi - \lambda < \theta < \pi - \lambda$. We ignore the small correction resulting from an integration of the signal over 2λ in the horizontal direction, as well as over the vertical direction, and assume that the entire signal comes from the center of the aperture at $\theta = \pi$. After the periodic steady state was reached, the O$_2$ desorption signal in the next cycle at $\theta = \pi$ was computed as a function of reaction time, $1/2r$, (Figure 17) for a 30-fold variation in f_O. Some of the parameters in Table 3 were varied so that the model reproduced the shape of the experimental O$_2$ desorption decay curves. The simulation results can be compared with the measurements in Figures 8−12. A sample set of measurements from Figure 10 (5 mTorr, 600 W) is included in Figure 17. The simulations correctly predict the observed fast initial falloff in D_b^{on} and slow long decay. In addition, the predicted small $\Delta[O(g)]$ relative to $\Delta[O_2(g)]$ (not shown) was consistent with the upper limit of $\sim 5\%$ for observed O desorption, relative to O$_2$. As observed, the simulated signals decay over a wider range at high O flux, compared to lower fluxes, although the simulations overpredict this trend.
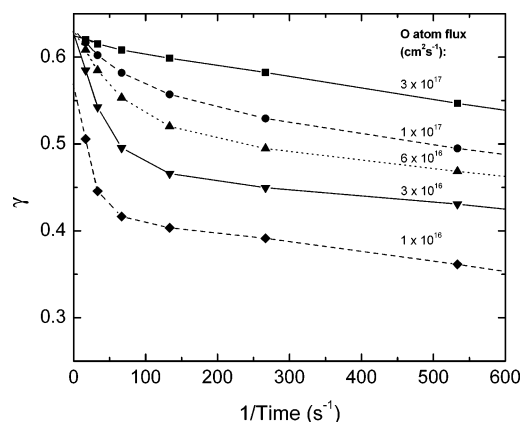
Recombination Reactions of Oxygen Atoms

J. Phys. Chem. B, Vol. 109, No. 44, 2005 **20997**

Figure 18. Simulations of O-atom recombination probabilities (γ) as a function of substrate rotation frequency. The extrapolation to zero rotation frequency provides the predicted value for γ in the plasma. The conditions are the same as those in Figure 17.

While the parameters in Table 3 are not unique or probably even the best set for accurately simulating the measured O_2 desorption, some trends can be derived from the simulations. The binding energy (E_{bm}) of mobile O is 10 kcal/mol and cannot be smaller than $\sim$9 kcal/mol (with $A_{dm} = 10^{13}$ s^{-1}) before O desorption becomes significant. Cartry et al.[37] observe a similar value of 12 kcal/mol for O recombination on silica. Negligible desorption of O occurs from the strongly adsorbed sites O(i), since $E_{ba}(i)$ is large (between 13 and 31 kcal/mol). Also, as reported for recombination of O on silica,[37] we find that [O_m] is too low for reaction 6 to be important. O_2 desorption arises mainly from reaction 7 with $i = 3-5$, corresponding to the peak in the adsorbed O coverage distribution. More weakly bound O(1) and O(2) are predominantly lost in reaction 5 to generate O_m.

A recombination coefficient, γ, can be computed from the ratio of the simulation flux to twice the computed O_2 desorption yield, over one full rotation after convergence.

$$\gamma = 1 - \frac{2\pi r}{\phi f_O} \int_{n/r}^{(n+1)/r} \{\sum_{i=1}^{n} k_{ma}(i)[O(i)][O_m] + k_{mm}[O_m]^2\}dt \quad (11)$$

These simulated values are given in Figure 18. The simulated γ extrapolated to infinitely long time (y-intercepts in Figure 18) provides values for anodized aluminum in the oxygen plasma. The extrapolated values are about 0.6 and are independent of O flux.

Very little has been reported on the recombination of O on anodized Al. On the basis of low O-atom densities observed in an oxygen plasma reactor with anodized Al walls, relative to when the walls were coated with SiO_2, Xu et al. have concluded that γ for anodized Al is much greater than that for SiO_2.[38] Gudmundsson et al. reported a low value of 0.05, derived from a global model that was adjusted to match measured O^+-to-O_2^+ ratios.[39] A much higher value ($\gamma = 1$) was used by the same group in the modeling of an oxygen plasma in a chamber composed of anodized Al, quartz, and plasma-oxidized Al.[40] In the present study, the model could reproduce the shape of the experimental O_2 decay curves with $s_m = 0$ (albeit with a factor of $\sim$3 higher than the measured O flux), yielding a γ of 0.3, but no combination of kinetic parameters could be found to match the decay curves and obtain the low value of $\gamma = 0.05$ reported by Gudmundsson et al.[39] The rough nature of the anodized Al surface could also contribute to the high values for γ in the present study.

Without studying the dependence of the O_2 desorption signals on the substrate surface temperature, it is not possible to quantitatively determine the dependence of γ on temperature. With the parameters in Table 3, the model qualitatively predicts that γ decreases (by $\sim$10%) when the temperature is increased (to 400 K), due to the increase in the rate of O desorption. This type of inverse temperature dependence is commonly observed for heterogeneous atom recombination.[9,10] γ is nearly independent of site density, decreasing by 5% when [S]$_0$ is decreased from 1×10^{15} to 2×10^{14} cm^{-2}.

Finally, we can estimate some potential influences of ion bombardment on O recombination. The experiments show that when O_2^+ flux is turned off by biasing the grids in front of the surface, the signal is not changed; hence, ion bombardment has no *short-term* effects on the kinetics. One can estimate at what flux ion bombardment might start to affect the instantaneous recombination kinetics. For example, ion bombardment might sputter O from the surface before it has a chance to recombine. Since the lifetime for adsorbed O is of the order of 0.02 s (the $1/e$ decay time of the O_2 signal in Figures 8−12), if the O coverage is 10^{15} cm^{-2}, then an ion dose of 10^{15} cm^{-2} in 0.02 s with an O sputter yield of 1 would result in sputtering competing with recombination for loss of adsorbed O. This ion flux requires an ion density of 2×10^{11} cm^{-3} near the wall (30 times higher than in the present study). Increasing the ion and electron density to this level by operating at a higher power and/or by reducing the plasma volume would also lead to a similar increase in O-atom density and its rate of heterogeneous recombination; hence, it is unlikely that ion bombardment would ever cause sputtering of adsorbed O in a mostly O_2 plasma. It is possible, however, that such an effect could occur in a dilute O_2 plasma. Longer-term effects of ion bombardment are much harder to evaluate. For example, ion bombardment could create surface sights for recombination that could be long-lived relative to the times explored in the biased grid experiments.

In future work, Auger electron spectroscopy will be added to measure time-resolved coverages. A radical beam source will also be added in the intermediate chamber so that recombination coefficients can be measured directly on the surface soon after it is exposed to the plasma. In addition, the temperature of the substrate will be varied, using a noncontact radiative heating/cooling method. With these added capabilities, the ability to extract kinetic parameters for a wide range of plasma−surface interactions by this spinning wall method will be greatly enhanced.

4. Conclusions

We have applied a new "spinning wall" method[26] to study O-atom recombination on anodized aluminum in an oxygen plasma. With this method, a cylindrical section of the wall of a plasma reactor is rotated, allowing the surface to be periodically exposed to the plasma and then analyzed by a differentially pumped quadrupole mass spectrometer a short time thereafter. By varying the substrate rotation frequency, the time between exposure of the surface to O atoms and the detection of desorbing O_2 can be varied. A model for O-atom recombination assumes adsorption occurs at surface sites with a range of binding energies. In the model, O detaches from these sites, becomes mobile, diffuses along the surface, and reacts with adsorbed O, leading to recombination and desorption of O_2. The model reproduces the observed shapes of the O_2 desorption decay curves and predicts a high O-atom recombination coefficient of 0.3−0.6 on anodized aluminum.

20998 *J. Phys. Chem. B, Vol. 109, No. 44, 2005*

Kurunczi et al.

References and Notes

(1) Lieberman, M. A.; Lichtenberg, A. J. *Principles of Plasma Discharges and Materials Processing*; John Wiley & Sons: New York, 1994.

(2) *Plasma Etching An Introduction*; Manos, D. M., Flamm, D. L., Eds.; Academic Press: Boston, MA, 1989.

(3) Mahorowala, A. P.; Sawin, H. H. *J. Vac. Sci. Technol., B* **2002**, *20*, 1077.

(4) Jin, W. D.; Sawin, H. H. *J. Vac. Sci. Technol., A* **2003**, *21*, 911.

(5) Lee, C.; Graves, D. B.; Lieberman, M. A. *Plasma Chem. Plasma Process.* **1996**, *16*, 99−120.

(6) Cunge, G.; Inglebert, R. L.; Joubert, O.; Vallier, L.; Sadeghi, N. *J. Vac. Sci. Technol., B* **2002**, *20*, 2137.

(7) Cunge, G.; Kogelschatz, M.; Sadeghi, N. *Plasma Sources Sci. Technol.* **2004**, *13*, 522.

(8) Cunge, G.; Kogelschatz, M.; Sadeghi, N. *J. Appl. Phys.* **2004**, *96*, 4578.

(9) Kota, G. P.; Coburn, J. W.; Graves, D. B. *J. Vac. Sci. Technol., A* **1998**, *16*, 270−277.

(10) Kota, G.; Coburn, J. W.; Graves, D. B. *J. Appl. Phys.* **1999**, *85*, 1.

(11) Fisher, E. R. *Plasma Sources Sci. Technol.* **2002**, *11*, A105.

(12) Capps, N. E.; Mackie, N. M.; Fisher, E. R. *J. Appl. Phys.* **1998**, *84*, 4376.

(13) Godfrey, A. R.; Ullal, S. J.; Braly, L. B.; Edelberg, E. A.; Vahedi, V.; Aydi, E. S. *Rev. Sci. Instrum.* **2001**, *72*, 3260.

(14) Ullal, S. J.; Singh, H.; Daugherty, J.; Vahedi, V. *J. Vac. Sci. Technol., A* **2002**, *20*, 1195.

(15) Herman, I. P.; Donnelly, V. M.; Guinn, K. V.; Cheng, C. C. *Phys. Rev. Lett.* **1994**, *72*, 2801−2804.

(16) Herman, I. P.; Donnelly, V. M.; Cheng, C. C.; Guinn, K. V. *Jpn. J. Appl. Phys.* **1996**, *35*, 2410−2415.

(17) Cheng, C. C.; Guinn, K. V.; Donnelly, V. M.; Herman, I. P. *J. Vac. Sci. Technol., A* **1994**, *12*, 2630−2640.

(18) Cheng, C. C.; Guinn, K. V.; Herman, I. P.; Donnelly, V. M. *J. Vac. Sci. Technol., A* **1995**, *13*, 1970−1976.

(19) Guinn, K. V.; Donnelly, V. M. *J. Appl. Phys.* **1994**, *75*, 2227−2234.

(20) Guinn, K. V.; Cheng, C. C.; Donnelly, V. M. *J. Vac. Sci. Technol., B* **1995**, *13*, 214−226.

(21) Bogart, K. H. A.; Donnelly, V. M. *J. Appl. Phys.* **2000**, *87*, 8351.

(22) Haverlag, M.; Oehrlein, G. S.; Vender, D. *J. Vac. Sci. Technol., B* **1994**, *21*, 96−101.

(23) Oehrlein, G. S.; Rembetski, J. F.; Payne, E. H. *J. Vac. Sci. Technol., B* **1990**, *8*, 1199−1211.

(24) Bell, F. H.; Joubert, O. *J. Vac. Sci. Technol., B* **1997**, *15*, 88−97.

(25) Graves, D. B.; Kushner, M. J. *J. Vac. Sci. Technol., A* **2003**, *21*, S152.

(26) Kurunczi, P. F.; Guha, J.; Donnelly, V. M. *Phys. Rev. Lett.*, submitted for publication, 2005.

(27) Malyshev, M. V.; Donnelly, V. M. *J. Appl. Phys.* **2000**, *87*, 1642.

(28) Donnelly, V. M. *J. Appl. Phys.* **1996**, *79*, 9353−9360.

(29) Brook, E.; Harrison, M. F. A.; Smith, A. C. H. *J. Phys. B* **1978**, *11*, 3115.

(30) McGuire, E. J. *Phys. Rev. A* **1971**, *3*, 267.

(31) Thompson, W. R.; Shah, M. B.; Gilbody, H. B. *J. Phys. B* **1995**, *28*, 1321.

(32) Kim, Y.-K.; Desclaux, J. P. *Phys. Rev. A* **2002**, *66*, 012708.

(33) Mark, T. D. *J. Chem. Phys.* **1975**, *63*, 1.

(34) Krishnakumar, E.; Srivastava, S. K. *Int. J. Mass Spectrosc. Ion Processes* **1992**, *113*, 1.

(35) Wetzel, R. C.; Baiocchi, F. A.; Hayes, T. R.; Freund, R. S. *Phys. Rev. A* **1987**, *35*, 559.

(36) Kim, Y. C.; Boudart, M. *Langmuir* **1991**, *7*, 2999.

(37) Cartry, G.; Magne, L.; Cernogora, G. *J. Phys. D: Appl. Phys.* **2000**, *33*, 1303.

(38) Xu, S. L.; Lill, T.; Podlesnik, D. *J. Vac. Sci. Technol., A* **2001**, *19*, 2893.

(39) Gudmundsson, J. T.; Kimura, T.; Lieberman, M. A. *Plasma Sources Sci. Technol.* **1999**, *8*, 22.

(40) Gudmundsson, J. T.; Marakhtanov, A. M.; Patel, K. K.; Gopinath, V. P.; Lieberman, M. A. *J. Phys. D: Appl. Phys.* **2000**, *33*, 1323.